ADVANCED MATERIALS
www.advmat.de

Terahertz Emission from Hybrid Perovskites Driven by Ultrafast Charge Separation and Strong Electron–Phonon Coupling

Burak Guzelturk, Rebecca A. Belisle, Matthew D. Smith, Karsten Bruening, Rohit Prasanna, Yakun Yuan, Venkatraman Gopalan, Christopher J. Tassone, Hemamala I. Karunadasa, Michael D. McGehee, and Aaron M. Lindenberg**

Unusual photophysical properties of organic–inorganic hybrid perovskites have not only enabled exceptional performance in optoelectronic devices, but also led to debates on the nature of charge carriers in these materials. This study makes the first observation of intense terahertz (THz) emission from the hybrid perovskite methylammonium lead iodide ($CH_3NH_3PbI_3$) following photoexcitation, enabling an ultrafast probe of charge separation, hot-carrier transport, and carrier–lattice coupling under 1-sun-equivalent illumination conditions. Using this approach, the initial charge separation/transport in the hybrid perovskites is shown to be driven by diffusion and not by surface fields or intrinsic ferroelectricity. Diffusivities of the hot and band-edge carriers along the surface normal direction are calculated by analyzing the emitted THz transients, with direct implications for hot-carrier device applications. Furthermore, photogenerated carriers are found to drive coherent terahertz-frequency lattice distortions, associated with reorganizations of the lead-iodide octahedra as well as coupled vibrations of the organic and inorganic sublattices. This strong and coherent carrier–lattice coupling is resolved on femtosecond timescales and found to be important both for resonant and far-above-gap photoexcitation. This study indicates that ultrafast lattice distortions play a key role in the initial processes associated with charge transport.

Lead-based hybrid organic– inorganic perovskites (HOIPs) have recently become extremely attractive among solution-processed semiconductors for optoelectronics.[1–3] In the last few years, these HOIPs have enabled exceptionally high power conversion efficiencies in solar cells owing to their remarkable photophysical properties.[4–6] For example, methylammonium lead iodide ($CH_3NH_3PbI_3$) (MAPI), one of the most studied HOIP prototypes, combines strong absorption in the visible range ($\alpha > 10^5$ cm^{-1}) with ultralong carrier diffusion lengths,[5,7,8] associated with long carrier lifetimes ($\tau > 100$ ns under 1-sun illumination) and modest carrier mobilities ($\mu \approx 10$–100 cm^2 V$^{-1} \cdot$ s^{-1}).[9–12] Unusually, slow carrier recombination and high defect tolerance in HOIPs have puzzled the community and led to scientific debates on the nature of charge carriers in these materials.[13–15] Theoretical works suggested the potential role of intrinsic ferroelectricity or bulk photovoltaic effects in the separation of charges,[16,17] while other studies have focused on the role of surface fields and diffusion.[18] Separately, carrier–lattice interactions[19–21] and large polaron formation[13,22,23] have been proposed to underpin the unique characteristics of the HOIPs. More recently, hot carriers in HOIP thin films were shown to exhibit enhanced in-plane transport,[24] which is attributed to long-lived hot carriers.[25–27] These aforementioned works highlight the crucial role of understanding the initial steps of charge separation and carrier–lattice coupling in HOIPs, which, on the other hand, has proven difficult to probe using conventional

Dr. B. Guzelturk, Prof. A. M. Lindenberg
Stanford Institute for Materials and Energy Sciences
SLAC National Accelerator Laboratory
Menlo Park, CA 94025, USA
E-mail: burakg@stanford.edu; aaronl@stanford.edu
R. A. Belisle, R. Prasanna, Prof. M. D. McGehee, Prof. A. M. Lindenberg
Department of Materials Science and Engineering
Stanford University
Stanford, CA 94305, USA
M. D. Smith, Prof. H. I. Karunadasa
Department of Chemistry
Stanford University
Stanford, CA 94305, USA
Dr. K. Bruening, Dr. C. J. Tassone
SSRL Materials Science Division
SLAC National Accelerator Laboratory
Menlo Park, CA 94025, USA
Y. Yuan, Prof. V. Gopalan
Department of Materials Science and Engineering
Pennsylvania State, University Park, PA 16802, USA
Prof. A. M. Lindenberg
Department of Photon Science
Stanford University and SLAC National Accelerator Laboratory
Menlo Park, CA 94025, USA

DOI: 10.1002/adma.201704737

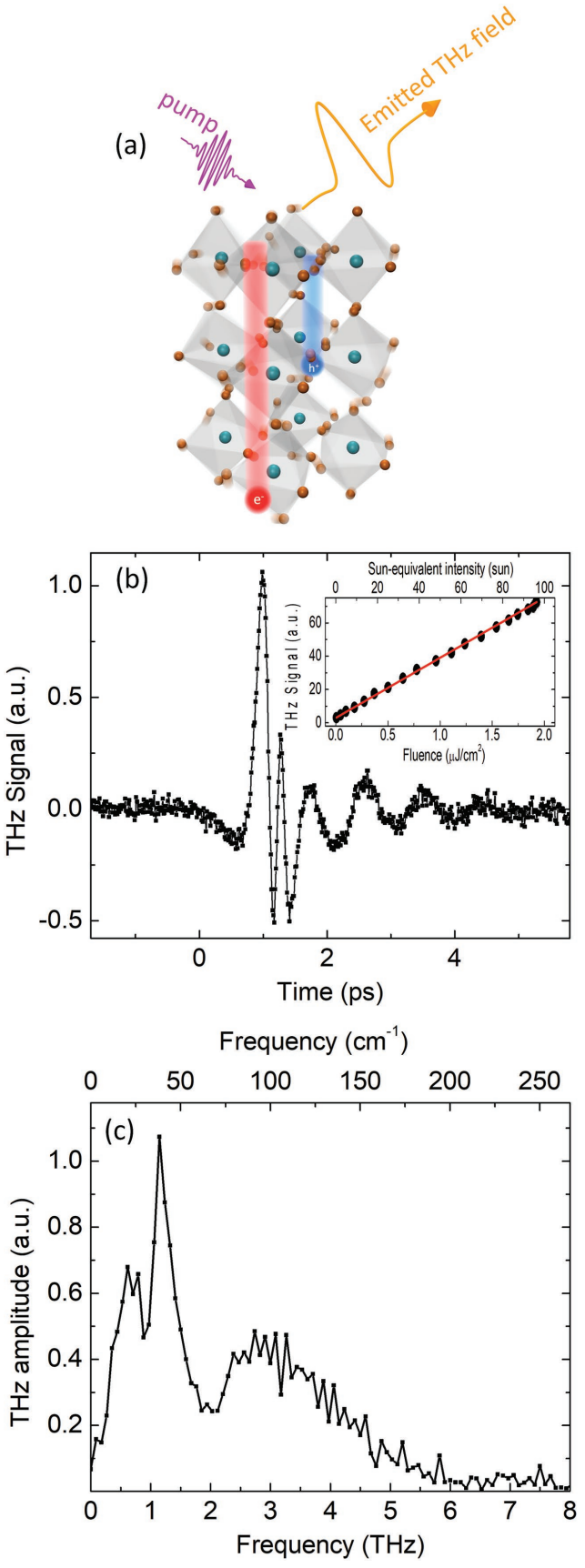

ultrafast techniques. In particular, real-time characterization of the out-of-plane motion of electrons and holes in perovskite films, which is directly relevant to solar cell performance, has not been carried out before.

Here, we make the first observation of intense terahertz (THz) emission from HOIPs following resonant or far-above-gap excitation, which enables a sensitive probe of the initial charge separation and carrier–lattice coupling in these materials under 1-sun-equivalent illumination conditions. We show that the emitted THz fields are generated by an ultrafast transient photocurrent normal to the film surface, arising from a difference in respective diffusivities of electrons and holes, a phenomenon known as the photo-Dember effect.[28] By resolving these radiated fields in the time domain, we find that the transient current points out of the film surface for far-above-gap excitation, associated with faster hot electron migration, whereas under resonant excitation, the hole diffusivity is found to be slightly larger than that of electrons. Furthermore, we show that surface-trap-mediated surface fields and intrinsic ferroelectricity do not play a key role in the initial charge separation in HOIPs and that this process is instead diffusion limited. Finally, analysis of the emitted THz amplitude spectra shows enhanced emission at terahertz frequencies associated with distortions of the inorganic octahedra as well as coupled organic–inorganic modes, indicative of strong carrier–lattice coupling for both band-edge and hot carriers. Resolving the emitted transients as a function of time, we uncover the dynamics of the coherent atomic-scale reorganizations associated with charge separation in hybrid lead-halide perovskites.

Figure 1a illustrates how an ultrafast photocurrent in the direction normal to the surface in turn causes emission of a burst of coherent quasi-single-cycle THz radiation. We detect this in a reflection geometry using phase-sensitive electrooptic sampling, also enabling simultaneous reconstruction of the frequency domain spectra (see Figure S1, Supporting Information and Experimental Section). Here, we tested polycrystalline MAPI thin films on glass substrates prepared by both spin coating and thermal evaporation techniques, which resulted in similar THz emission properties (e.g., amplitude, field polarity, and also spectrum). We also observed THz emission in other hybrid perovskites (e.g., $MAPbBr_3$ and $FA_{0.83}Cs_{0.17}PbBr_xI_{3-x}$; $FA = (H_2N)_2CH^+$, $x = 0.17$) as well as the all-inorganic $CsPbBr_3$ (see Figure S2, Supporting Information); here we focus on the prototypical MAPI thin films.

Upon photoexcitation with a 50 fs 400 nm laser pulse (2 μJ cm^{-2}), we detected a quasi-single-cycle THz transient as shown in Figure 1b. A 0.25 mm thick GaP was used as the electrooptic detector with bandwidth up to 8 THz,[29] and the setup was purged with nitrogen. The emitted THz electric field amplitude is shown in Figure 1b. At $t \approx 0$ ps, we observe the

Figure 1. a) Schematic illustration of the THz emission from $CH_3NH_3PbI_3$ (MAPI). Following photoexcitation, a burst of THz radiation is detected in a reflection geometry encoding the time-dependent currents and charge–lattice coupling processes that occurs following photoexcitation. b) Time-domain THz electric field emitted by MAPI thin film upon excitation with 400 nm fs light pulse at a fluence of 2 μJ cm^{-2}. Inset shows the THz signal amplitude as a function of pump fluence and the corresponding sun-equivalent intensity. c) Amplitude spectrum of the emitted THz field exhibiting three distinct peaks at 0.65, 1.2, and 2.8 THz.

build-up of an emission feature which is immediately followed by a faster oscillatory transient and then another slower feature that coherently rings for ≈4 ps. To resolve these different modes, we investigate the amplitude spectrum of the emitted field as shown in Figure 1c. The initial slower component gives rise to a broad peak centered at 0.65 THz. The faster transient results in a broader peak at 2.8 THz, while the ringing feature generates a sharp peak at 1.2 THz. These higher frequency modes at 1.2 and 2.8 THz match known vibrational modes of the hybrid structure and will be discussed in detail later in this manuscript. The inset of Figure 1b shows the radiated THz field amplitude as a function of pump fluence, which increases linearly in the range from 8 nJ cm^{-2} to 2 μJ cm^{-2} (see the linear fit in the inset), hence spanning from less than 1-sun equivalent intensity up to ≈100-sun equivalent intensity (see the Supporting Information), corresponding to photogeneration conditions relevant to normal solar cell operation.

Figure 2a shows the THz intensity transmitted through an analyzing polarizer with varying angle Φ (see Figure 2a inset)

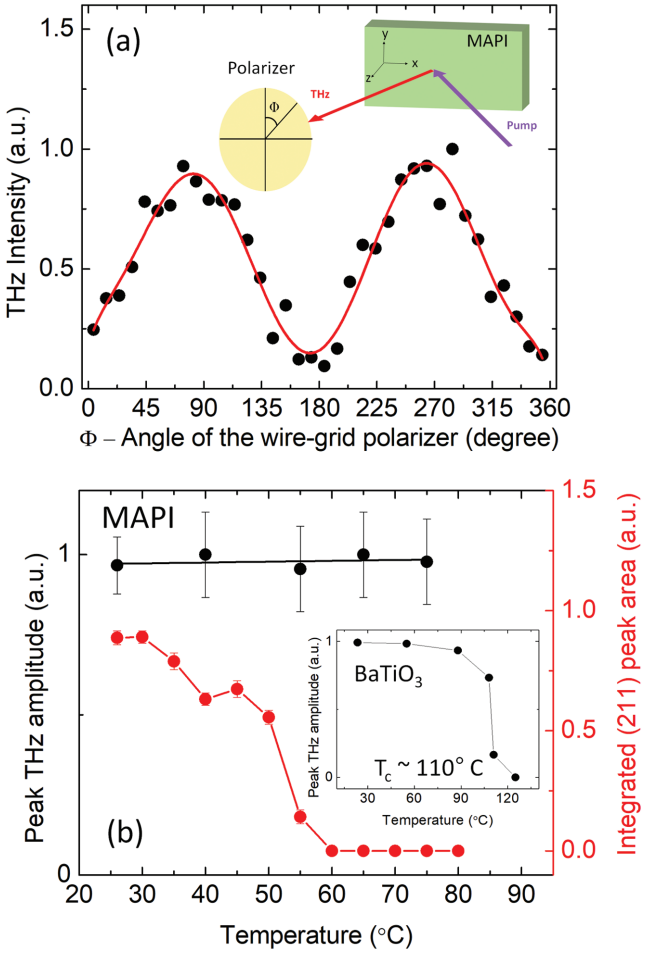

Figure 2. a) Polarization dependence of the emitted THz fields. Inset illustrates the polarization characterization setup and the polarizer angle Φ. b) THz signal amplitude (shown in black) and integrated area under (211) peak from X-ray diffraction measurements (shown in red) as a function of temperature. Tetragonal-to-cubic phase transition occurs at around ≈60 °C. Inset shows similar measurement in prototypical ferroelectric $BaTiO_3$ showing sensitivity to ferroelectric-to-paraelectric transition.

detected using a cryogenic hot-electron bolometer. The THz intensity is maximized for Φ = 90° and 270° indicating that the emitted THz field is p-polarized (parallel to the plane of incidence). Thus, there is no net component of the transient current along the *y* direction (see Figure 2a inset). The polarization of the THz field is also independent of the polycrystalline sample orientation (see Figure S3, Supporting Information); hence, the net in-plane (*x* and *y*) current is zero. Thus, we conclude that the net transient photocurrent, which gives rise to the THz emission, is along the surface normal direction. Also, Figure S4 (Supporting Information) shows that the emitted THz field amplitude is independent of the polarization of the pump beam as expected for a polycrystalline film with an ensemble of domain orientations.

We now consider potential mechanisms that underpin the observed THz electromagnetic radiation from MAPI thin films. Previously, intrinsic ferroelectricity in tetragonal MAPI has been proposed to cause efficient charge separation as in a p–n junction due to a photoferroic effect[16] or shift current.[17] To test the role of ferroelectricity, we investigated the temperature dependence of the THz emission. While increasing the temperature from 25 to 75 °C across the tetragonal-to-cubic phase transition, we did not observe any discernible change in the THz signal amplitude as shown in Figure 2b. X-ray diffraction measurements probing the (211) reflection on MAPI thin films confirm this tetragonal to cubic transition at ≈60 °C (see Figure 2b), consistent with prior measurements.[30] Therefore, insensitivity of the emitted THz field across the tetragonal-cubic phase boundary suggests that the initial charge separation process in MAPI is not related to ferroelectricity or to a related bulk photovoltaic response, which would require a polar non-centrosymmetric structure extending across the entire probed region of the polycrystalline film.[17] In contrast, control measurements in the prototypical ferroelectric $BaTiO_3$ show total suppression of the emitted THz field above the ferroelectric–paraelectric transition at ≈110 °C (see the inset of Figure 2b).

Other possible THz emission mechanisms[31] from semiconductor surfaces have been identified as built-in surface fields (or depletion fields),[32–34] the photo-Dember effect,[33,35] and second-order nonlinear polarization (i.e., optical rectification effect).[36,37] Previously, THz emission from GaAs was observed because of a built-in depletion field,[32] creating a surge current along the field direction following photoexcitation. Alternatively, the photo-Dember effect, which dominates the THz emission from InSb and InAs,[28] leads to formation of a transient dipole due to different diffusivities of electrons and holes. To assess these different mechanisms, we excited the MAPI thin films at different excitation energies and employed a 1 mm piece ZnTe as the electrooptic crystal since it provides almost an order of magnitude higher signal intensity than that of the 0.25 mm GaP crystal. **Figure 3**a shows the emitted THz field amplitudes measured for excitation wavelengths at 400, 770, and 790 nm (see the inset of Figure 3a for the absorption profile of the MAPI thin film). Under 790 nm excitation, we do not observe any measurable THz emission within our detection capability. In this case, there is no considerable carrier generation since the excitation energy is well below the band gap of MAPI. This implies that the THz emission emerges from photogenerated carriers; thus, we can rule out an optical rectification effect (see also Figure S11, Supporting Information).

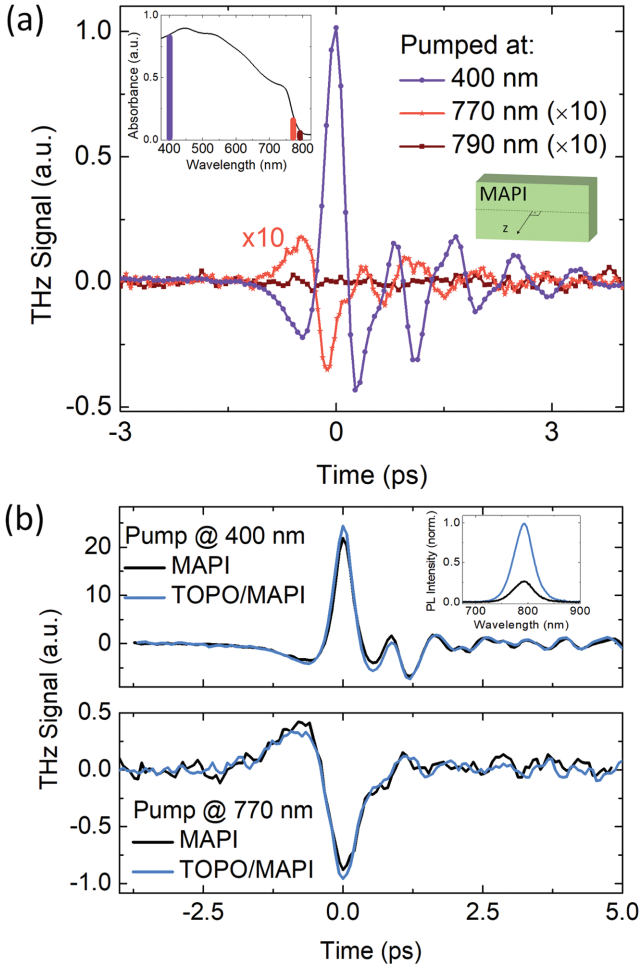

Figure 3. a) The emitted THz signals when the MAPI is excited at 400, 770, and 790 nm. There is no measurable signal for the 790 nm excitation. The THz signal amplitude is more than an order of magnitude larger when pumped with 400 nm. Polarity of the THz field is reversed when pumping with 770 nm as compared to that when pumped with 400 nm light, indicating that the direction of the initial charge separation is reversed. Inset shows the absorbance of the MAPI thin film marked with the positions of the excitation wavelengths. The excitation photon fluxes are 0.47×10^{13}, 1.67×10^{13}, and 4.16×10^{13} photons cm^{-2} for 400, 770, and 790 nm, respectively. b) THz emission signals from bare and TOPO-treated MAPI thin films. Top and bottom panels show the emitted THz signals under 400 and 770 nm excitation, respectively. Emitted THz transients do not change upon surface treatment. Inset in the top panel shows the steady state photoluminescence of the MAPI films before and after TOPO treatment, indicating threefold increase in the photoluminescence intensity.

In Figure 3a, we note remarkable differences in the emitted THz signals when the sample is excited at 400 nm versus 770 nm. First, the THz signal amplitude is more than an order of magnitude larger when using 400 nm light. This observation is consistent with either a surface-field or a photo-Dember model. In the former, higher energy photons deposit energy closer to the surface leading to an enhanced surface sensitivity. In the latter, hot carriers exhibit higher effective diffusion coefficients leading to enhanced charge separation and the build-up of a local field. However, it is also observed that the polarity of the THz field is reversed between 400 and 770 nm excitation. Polarity reversal indicates that the direction of the transient current is inverted upon changing the excitation wavelength. Therefore, THz emission cannot be self-consistently explained by only a surface-field effect. However, surface-field and photo-Dember effects may coexist. To check this hypothesis, we investigated surface treatments, which can reduce the surface state/trap density, and thus effectively modify surface fields. Recently, Lewis bases such as tri-*n*-octylphosphine oxide (TOPO) were shown to passivate MAPI film surfaces leading to a significantly increased photoluminescence emission quantum yield.[38] Here, we applied TOPO treatment on the MAPI thin films (see Experimental Section). After the treatment, we achieved threefold increase in the photoluminescence intensity (see the inset of Figure 3b). Also, the time-resolved fluorescence decay slowed down considerably after the treatment (see Figure S5, Supporting Information) due to suppression of nonradiative recombination at the top surface. Figure 3b shows the THz signals measured from bare and TOPO-treated MAPI thin films under 400 and 770 nm excitations. Contrary to the surface-field hypothesis, we do not observe any quantitative change in the THz emission although the surface treatment has effectively increased the surface passivation as understood from the photoluminescence properties. Previously, THz emission from a GaAs surface, well-known surface-field emitter, has shown strong modification upon surface passivation due to the suppression of surface state density which leads to an unpinning of the Fermi level, hence decreased surface fields.[39] Overall, absence of any modification of the THz emission upon surface passivation in MAPI thin films implies that surface states and associated surface fields do not play a crucial role either in the THz emission or charge separation(see the Supporting Information). Photoelectron measurements in MAPI thin films showed negligible band bending for the bare MAPI surface before.[40] In contrast, band bending and Fermi level pinning were shown to occur at the interfaces where MAPI is in contact with charge transport materials, such as indium tin oxide (ITO), poly(3,4-ethylenedioxythiophene) polystyrene sulfonate (PEDOT:PSS), TiO_2, and MoO_3 due to charge redistribution across the interface.[18,40]

The transient current generated due to the photo-Dember effect can be expressed as $J_{\text{Dember}} = J_{\text{n}} + J_{\text{p}}$, where $J_{\text{n}} = -eD_{\text{n}}\frac{\partial \Delta n}{\partial z}$ and $J_{\text{h}} = eD_{\text{p}}\frac{\partial \Delta p}{\partial z}$ are the transient currents arising from the diffusion of electrons and holes, respectively.[41] Here, D is the diffusivity that can be expressed in terms of Einstein's relation; $D = k_{\text{B}}T\mu/e$, where k_{B} is the Boltzmann constant, T is the carrier temperature, and μ is the carrier mobility. $\frac{\partial \Delta n}{\partial z}$ represents the spatial gradient of the photogenerated carriers along the film thickness, which is equal to $-N_0\alpha e^{-\alpha z}$, where N_0 is the peak carrier density and α is the absorption coefficient. We can write: $J_{\text{Dember}} = -e\Delta D\frac{\partial \Delta n}{\partial z}$, where $\Delta D = \frac{k_{\text{B}}}{e}(\mu_{\text{p}}T_{\text{p}} - \mu_{\text{n}}T_{\text{n}})$.

We calibrated the polarity of the emitted THz fields by referencing to that of a bulk InAs crystal (see Figure S6, Supporting Information), a well-established photo-Dember emitter.[28] In InAs, the transient current always points out of the surface since electrons have much higher mobility than holes. Under 770 nm excitation, the polarity of the THz transient emitted by the MAPI film is opposite to that of InAs. This indicates that band-edge holes in MAPI are more diffusive than band-edge electrons. Since excess kinetic energy is negligible ($T_{\text{p}} = T_{\text{n}}$) in this

excitation condition, then $\mu_p > \mu_n$. Although some theoretical studies predicted slightly larger electron mobilities before,[42] independent experimental reports have recently measured hole mobility in MAPI single crystals to be ≈1.3–4 times larger than electron mobility,[43,44] qualitatively agreeing with our finding. In the case of 400 nm excitation, the polarity of the THz emission is inverted with respect to the 770 nm case, with the same polarity as of InAs. This indicates that hot electrons diffuse faster than hot holes ($D_n > D_p$). Taking into account $\mu_p > \mu_n$, this implies that the excess kinetic energy of the hot electrons is larger than that of hot holes ($T_n > T_p$). For this, the carrier mobilities are considered to be independent of the excitation energy. This assumption is supported by previous time-resolved THz conductivity measurements,[10,11] which did not observe any change in the conductivity decays within the first ≈1 ns time window for different excitation energies. This suggests that hot carriers (excited by 400 nm) possess the same mobility as the band-edge carriers in the MAPI.

To relate the emitted THz electric field amplitude to the photo-Dember current, we considered a surface current density since the region where photoinduced current flows is considerably smaller than the wavelength of the emitted THz field (≈300 μm).[45] Then, $E_{THz} = \eta \frac{J_{Dember} d}{\varepsilon_0 c}$, where E_{THz} is the emitted THz field amplitude, d is the penetration depth of the photogenerated carriers (i.e., absorption length), and η is an outcoupling coefficient. Since the current is assumed to be a surface current sheet ($J_{Dember} \times d$), we can use ε_0 as the dielectric permittivity and c as the speed of light. By using the complex dielectric function of the MAPI,[46] we determined η to be ≈1% due to the large refractive index ($n_r > 6$) of the MAPI thin film in the THz range[46] (see Figure S7, Supporting Information for the outcoupling coefficients). We can express the emitted field $E_{THz} = \eta e \frac{\Delta D N_0 (1 - e^{-1})}{\varepsilon_0 c}$, where ΔD is the difference in the carrier diffusivities, and N_0 is the peak carrier density. $(1 - e^{-1})$ is due to a depth-dependent averaging of the carrier density gradient (see Supporting Information for the details of the Calculations). We experimentally measured E_{THz} as 0.34 V cm^{-1} under 400 nm excitation at a fluence of ≈2 μJ cm^{-2} resulting in $N_0 \approx 10^{18}$ cm^{-3}. Hence, we find $\Delta D_{400\,nm} = \frac{k_B}{e}(\mu_n T_n - \mu_p T_p) = 0.89\,cm^2 s^{-1}$ **(1)**. After normalizing the THz field amplitudes by the incoming photon flux and also carrier gradient depths, we find that $E_{THz}(400\,nm) = -8.8 \times E_{THz}(770\,nm)$. Here, the negative sign is due to the observed polarity reversal between two excitation conditions. Hence, $\frac{k_B}{e}(\mu_n T_n - \mu_p T_p) = 8.8 \times \frac{k_B}{e}(\mu_p T_{300K} - \mu_n T_{300K})$ **(2)**. Here, T_n and T_p are the excess energy of the electrons and holes imparted by the 400 nm excitation, respectively. Total excess energy in this condition is ≈1.45 eV (difference in the photon energy and the band gap), thus $T_n + T_p = 16\,731$ K **(3)**. In the case of 770 nm excitation, the carrier temperature for both electron and hole is assumed to be 300 K. Finally, we employed the reported THz mobility of MAPI thin films as $\mu_n + \mu_p = 25$ cm^2 V$^{-1} \cdot$ s^{-1} **(4)** from ref. [10]. By solving **1–4**, we find $\mu_n = 10.55$ cm^2 V$^{-1} \cdot$ s^{-1}, $\mu_p = 14.45$ cm^2 V$^{-1} \cdot$ s^{-1}, $T_n = 10\,084$ K and $T_p = 6647$ K. Previously, the sum of carrier mobilities ($\mu_n + \mu_p$) have been measured and reported via time-resolved microwave or THz conductivity[10,11,47,48] Here, THz emission spectroscopy allows for direct noncontact and high time resolution access to the individual carrier mobilities when combined with the time-resolved conductivity since the THz emission is complimentarily sensitive to the difference in the carrier mobilities in the MAPI thin films. The uncertainty in these individual carrier mobilities and hot carrier temperatures arises from the assumptions (e.g., excited carrier density, effective electron and hole temperatures, and prior measurement of the sum of the carrier mobilities) that we made for this calculation, rather than the experimental error in the measurement of the THz field amplitudes.

Under resonant excitation, $D_{n,770\,nm} = 0.27$ cm^2 s^{-1} and $D_{p,770\,nm} = 0.37$ cm^2 s^{-1}. Thus, the band-edge carriers could diffuse ≈6 nm in the first picosecond after the photoexcitation. Recently, Hill et al.[49] reported in-plane diffusivity of near resonantly excited carriers in MAPI thin films as ≈1 cm^2 s^{-1}, which agrees very well with our reported diffusivity value ($D \approx 0.64$ cm^2 s^{-1}) found for band-edge carriers. In the case of 400 nm excitation, we find larger diffusivities due to the increased carrier temperature of the hot carriers: $D_{n,400\,nm} = 9.17$ cm^2 s^{-1} and $D_{p,400\,nm} = 8.28$ cm^2 s^{-1}. A picosecond after photoexcitation, hot electrons, and hot holes have migrated on average 30 and 28 nm, respectively. Hence, hot electrons diffuse 2 nm longer than hot holes do in the first picosecond before the hot carriers are completely thermalized. Therefore, hot-carrier transport along surface normal is dominated by the hot electrons in MAPI thin films. Hot-carrier diffusivities reported here are found to be an order of magnitude smaller than those of ref. [24], which used transient absorption microscopy to probe in-plane hot-carrier diffusivity. This might be related to the differences in the properties of the employed samples, in-plane versus out-of-plane response, or to the differences in the overall approaches to extract these values. Hot-carrier extraction offers an exciting opportunity to boost the power conversion efficiencies in solar cells beyond the Shockley–Queisser limit. Therefore, direct access to the individual hot-carrier diffusivities will be important for designing and implementing devices that can effectively harvest hot carriers.

Finally, we show that the emitted THz transients enable a sensitive real-time probe for carrier–lattice coupling in the hybrid perovskites. Previously, carrier-induced lattice distortions have been claimed to underpin the efficient hot-carrier transport, high defect tolerance, and long carrier lifetimes in these materials.[14,19,22,23,50] In **Figure 4**a,d, we first show the amplitude spectrum of the emitted THz fields for 400 and 770 nm excitations, respectively. The amplitude spectrum when excited by 400 nm exhibits three peaks at 0.65, 1.2, and 2.8 THz as noted above. Here, we will first focus on the 1.2 THz mode, then we will discuss 2.8 and 0.65 THz modes later. The sharp peak at 1.20 THz (40 cm^{-1}) coincides with a longitudinal optical (LO) phonon mode of MAPI, associated with I-Pb-I angular distortions of the inorganic framework.[46,51] The broader peak at 2.8 THz (92 cm^{-1}) matches well with the coupled vibration modes between the inorganic and organic sublattices, associated with the collisions of the organic cation with the inorganic sublattice.[52] Previously, the THz emission spectrum from polar semiconductors (Te,[53] PbTe,[54] and InSb[55]) was shown to exhibit enhanced emission at LO phonon modes arising from charge displacements coherently coupling with the lattice vibrations.[53,56] Our observation

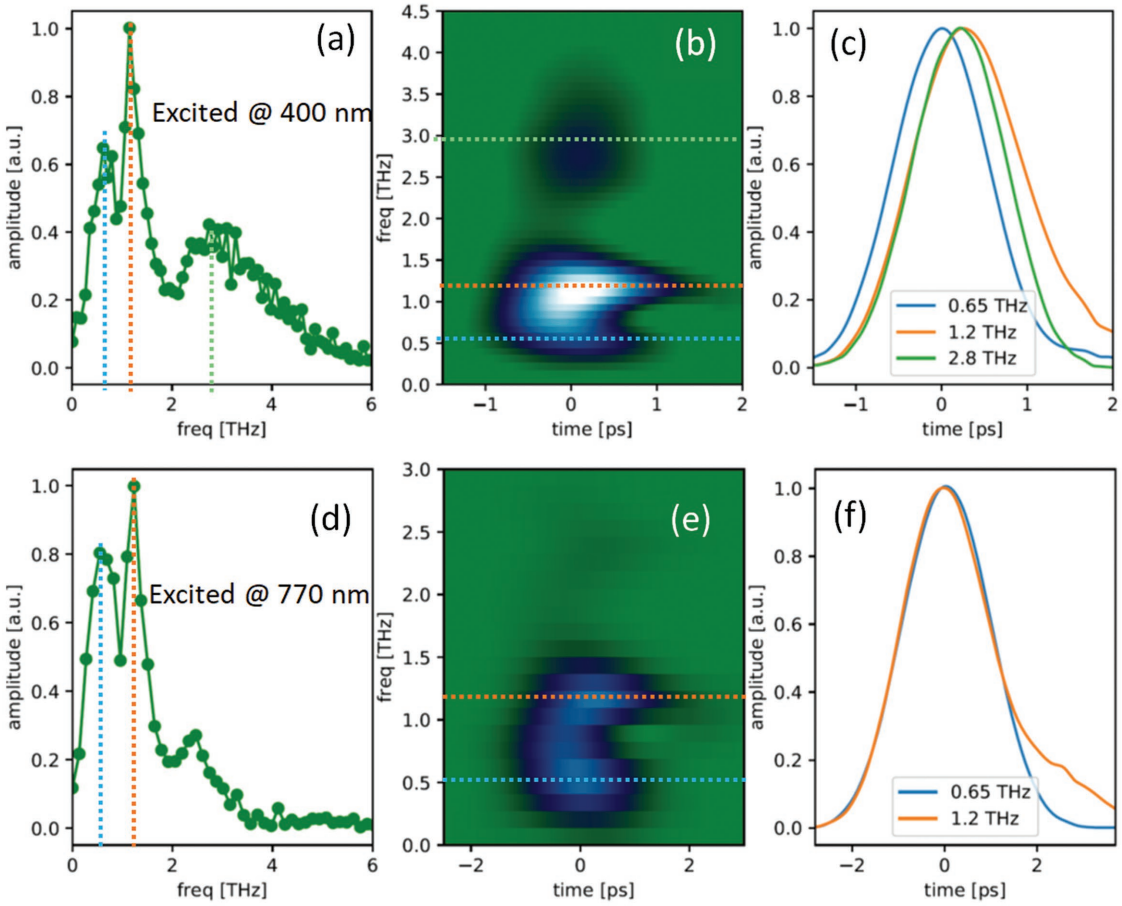

Figure 4. Amplitude spectrum of the emitted THz field under a) 400 nm and d) 770 nm excitation. Short-time Fourier transform analysis of the THz field under b) 400 nm and e) 770 nm excitation. Time evolution of the amplitude signals at 0.65, 1.20, and 2.80 THz in (c) 400 nm and (f) 770 nm excitation cases. In the case of 400 nm excitation, higher frequency modes arising from the carrier–lattice coupling are observed with a time delay with respect to the initial burst of THz radiation. In the case of 770 nm excitation, excitation of the 1.2 THz mode is instantaneous within the experimental time resolution.

therefore indicates that photogenerated carriers in MAPI strongly couple to (and drive) coherent lattice vibrations as inferred from these modes in the emitted THz spectrum. We note that the real part of the complex dielectric function in MAPI was shown to dip around 1.2 THz;[46] this in turn is expected to reduce screening of the internal fields and lead to stronger coupling of the carriers to the lattice as well as stronger outcoupling of the THz emission at this frequency. In the case of 770 nm excitation, due to small signal amplitudes, we employed 1 mm ZnTe for the electrooptic detection. Thus, the bandwidth of the emission is limited to ≈2.5 THz and hence we focus on the response of the 1.2 THz mode in this case (see Figure S8, Supporting Information for the 400 nm excitation case measured using a 1 mm ZnTe detector). Figure 4d shows that the 1.2 THz mode is also excited under resonant pumping (770 nm excitation). Therefore, strong coupling to the lattice mode at 1.2 THz (LO phonon of the inorganic sublattice) is observed under both resonant and far-above-gap excitation wavelengths. Thus, our observation shows direct evidence for strong coupling of the photoexcited carriers to the lattice, which was suggested to underlie the emergent optoelectronic properties of the metal-halide perovskites.[24,57]

Figure 1b shows that these vibrational excitations are associated with a complex time-dependent response in which the build-up of the THz transient (associated with the build-up of the Dember field) leads to oscillatory responses involving first fast and then slower timescales. Therefore, we investigate the time evolution of the amplitude spectrum of the emitted THz field transients via a short-time Fourier transform analysis, allowing us to identify the coupling dynamics between the photogenerated carriers and the lattice vibrations observed. Figure 4b,e shows the evolution of the THz amplitude spectrum in time for the far-above-gap and resonant excitation conditions, respectively. In Figure 4c,f, we show the time evolution of the measured emission peaks of 1.2 and 2.8 THz modes. Notably, the analysis reveals that the higher energy emission peaks turn on with a time delay in the case of far-above-gap excitation. Both the 1.2 and 2.8 THz modes turn on ≈250 fs after the main emission peak at ≈0.65 THz. We note that the observed time delay for the emergence of the 1.2 and 2.8 THz modes (≈250 fs) is comparable to that observed for the initial cooling of hot electrons as measured by time-resolved two-photon photoelectron spectroscopy and is in accordance with a proposed competition between hot carrier relaxation and polaron formation as

proposed in ref. [27]. We attribute the first broad peak centered at 0.65 THz as reflective of the Dember-field response of the free carriers before they are able to drive coherent lattice oscillations.[53,54] After the fast initial cooling of the hot carriers, excitation of the coherent lattice modes take place, which persist for 3–4 ps as in the case of the 1.2 THz mode. In the case of resonant excitation, on the other hand, the coherent excitation of the LO phonons takes place almost instantaneously and we do not resolve any time delay within our time resolution (i.e., 50 fs), suggesting that excitation of this coherent mode proceeds much faster. In the case of resonant excitation, there is no competition due to carrier cooling; hence, coherent coupling to the LO phonons occurs much faster. Figure S9 (Supporting Information) shows the THz amplitude spectra as a function of excitation fluence. The 1.2 THz peak shows a linear response with increasing excitation fluence (Figure S9c, Supporting Information), highlighting that the coherent lattice excitation observed here is an intrinsic property of MAPI. This coherent excitation of the lattice vibrations is valid even for 1-sun-equivalent excitation conditions; thus, the coherent LO phonon excitation observed here is relevant to the photovoltaic applications and carrier dynamics of the hybrid perovskites.

Our findings indicate that electron–optical phonon coupling in MAPI is strong and dominates the early time processes associated with charge transport, rather than the acoustic modes which have previously been hypothesized to dominate this process.[12–14] However, we emphasize that the coherent oscillatory response observed is associated with a coherent lattice response in which each excited vibrational mode is coherent across unit cells and not with incoherent carrier–LO coupling as typically occurs during hot carrier cooling. The observed coherent lattice response may therefore be associated with recent reports of large polaron formation and light-induced structural modifications.[19,22] From this perspective, these measurements capture the timescale for the formation of these light-induced structural deformations. In the case of resonant band-edge excitation, these measurements show that lattice distortions occur also for the band-edge carriers, whose properties are of key importance with respect to photovoltaic device performance. The strong coupling of the carriers to the lattice vibrations could underpin the surprising optoelectronic properties, such as long carrier lifetimes and high defect tolerance as well as modest carrier mobilities in the hybrid perovskites.

In summary, we describe a new approach toward characterizing ultrafast charge separation and coupled carrier–lattice structural distortions in the hybrid perovskites under device-relevant excitation conditions. These measurements enable characterization of individual carrier diffusivities in the out-of-plane direction in thin films with sensitivity to hot-carrier transport and eliminate the proposed roles of ferroelectricity and surface fields in the initial charge separation processes. The THz emission spectra reveal significant structural distortions that accompany charge separation, important with respect to understanding the unique optoelectronic properties of these materials. Moreover, considering the large terahertz emission amplitudes comparable to that of single-crystal semiconductors and calculated high optical-to-THz conversion efficiencies ($\approx 10^{-3}$), hybrid perovskites could enable high-efficiency, large-area, low-cost, and broadband THz emitters using lateral Dember fields to boost outcoupling of the THz fields.[35] Monitoring THz emission as presented here could provide valuable insights into in situ carrier and lattice dynamics in complex device structures while providing all-optical access to degradation mechanisms in the hybrid perovskites.

Experimental Section

Preparation of MAPI Thin Films and Application of TOPO Treatment: Glass substrates were cleaned by subsequent sonication in diluted Extran solution (EMD, EX0996-1), acetone (EMD, AX0115-1), and isopropanol (IPA) (EMD, PX1835P-4) followed by UV ozone irradiation for >5 min. A 0.88 M solution of lead (II) acetate trihydrate (Sigma-Aldrich, 99.999%):methylammonium iodide (Dyesol) at a 1:3 ratio in *N*,*N* dimethyl formamide (Acros, 99.8%) was prepared in a nitrogen environment. The solution was filtered through a 0.2 µm polytetrafluoroethylene (PTFE) filter immediately before spin coating at 2000 rpm for 60 s in a dry air environment. Samples were left at room temperature for 10 min and then annealed at 100 °C for 5 min.

For TOPO (Sigma-Aldrich >99%) treated samples, a 0.025 M solution of TOPO in chlorobenzene was prepared and spin coated onto prepared perovskite films at 4000 rpm for 45 s.

THz Emission Setup: The experimental setup is schematically depicted in Figure S1 (Supporting Information). We used a long cavity Ti:sapphire oscillator with center wavelength of 795 nm and a full-width at half-maximum of ≈30 nm. The repetition rate of the laser is 5.12 MHz and the pulse duration is 50 fs. For 400 nm excitation, we doubled the output of the laser by using a beta barium borate (BBO) crystal and used a 400 nm band-pass filter to block the remaining 800 nm beam.

We excited the samples at an incident angle of 45° with respect to surface normal of the films. The excitation spot on the sample was ≈1 mm^2. The excitation beam was chopped at 320 kHz using an acousto-optic modulator. Using off-axis parabolic mirrors, the emitted THz fields in reflection mode were directed into an electrooptic crystal (1 mm ZnTe). Approximately 1% of the laser output was used as an electrooptic sampling beam. The THz field transients were detected by monitoring the output of the balanced detector using a lock-in amplifier while scanning the optical delay stage for the sampling beam.

To characterize the polarization state of the emitted THz fields, we employed a THz wire-grid polarizer in between the sample and the hot-electron bolometer.

Supporting Information

Supporting Information is available from the Wiley Online Library or from the author.

Acknowledgements

The terahertz spectroscopy work was supported by the Department of Energy, Basic Energy Sciences, Materials Sciences, and Engineering Division. The preparation of the samples was supported by the National Science Foundation. M.D.S. is supported by an NSF graduate fellowship (DGE-114747). The work by M.D.S. and H.I.K. was funded by the SLAC National Accelerator Laboratory. The collaboration between Y.Y., V.G., and A.M.L. on the THz emission from $BaTiO_3$ crystals was supported by the Department of Energy grant number DE-SC0012375.

Conflict of Interest

The authors declare no conflict of interest.

Keywords

carrier–lattice coupling, charge separation, hybrid organic–inorganic perovskites, $MAPbI_3$, THz emission, ultrafast structural dynamics

Received: August 19, 2017
Revised: December 21, 2017
Published online: January 23, 2018

[1] M. M. Lee, J. Teuscher, T. Miyasaka, T. N. Murakami, H. J. Snaith, *Science* **2012**, *338*, 643.
[2] Z.-K. Tan, R. S. Moghaddam, M. L. Lai, P. Docampo, R. Higler, F. Deschler, M. Price, A. Sadhanala, L. M. Pazos, D. Credgington, F. Hanusch, T. Bein, H. J. Snaith, R. H. Friend, *Nat. Nanotechnol.* **2014**, *9*, 687.
[3] G. Xing, N. Mathews, S. S. Lim, N. Yantara, X. Liu, D. Sabba, M. Grätzel, S. Mhaisalkar, T. C. Sum, *Nat. Mater.* **2014**, *13*, 476.
[4] T. M. Brenner, D. A. Egger, L. Kronik, G. Hodes, D. Cahen, *Nat. Rev. Mater.* **2016**, *1*, 15007.
[5] M. A. Green, A. Ho-Baillie, H. J. Snaith, *Nat. Photonics* **2014**, *8*, 506.
[6] J. S. Manser, J. A. Christians, P. V. Kamat, *Chem. Rev.* **2016**, *116*, 12956.
[7] G. Xing, N. Mathews, S. Sun, S. S. Lim, Y. M. Lam, M. Grätzel, S. Mhaisalkar, T. C. Sum, *Science* **2013**, *342*, 344.
[8] S. D. Stranks, G. E. Eperon, G. Grancini, C. Menelaou, M. J. P. Alcocer, T. Leijtens, L. M. Herz, A. Petrozza, H. J. Snaith, *Science* **2013**, *342*, 341.
[9] M. B. Johnston, L. M. Herz, *Acc. Chem. Res.* **2016**, *49*, 146.
[10] C. S. Ponseca, T. J. Savenije, M. Abdellah, K. Zheng, A. Yartsev, T. Pascher, T. Harlang, P. Chabera, T. Pullerits, A. Stepanov, J.-P. Wolf, V. Sundstrom, *J. Am. Chem. Soc.* **2014**, *136*, 5189.
[11] C. Wehrenfennig, G. E. Eperon, M. B. Johnston, H. J. Snaith, L. M. Herz, *Adv. Mater.* **2014**, *26*, 1584.
[12] M. Karakus, S. A. Jensen, F. D'Angelo, D. Turchinovich, M. Bonn, E. Cánovas, *J. Phys. Chem. Lett.* **2015**, *6*, 4991.
[13] X.-Y. Zhu, V. Podzorov, *J. Phys. Chem. Lett.* **2015**, *6*, 4758.
[14] A. D. Wright, C. Verdi, R. L. Milot, G. E. Eperon, M. A. Pérez-Osorio, H. J. Snaith, F. Giustino, M. B. Johnston, L. M. Herz, *Nat. Commun.* **2016**, *7*, 11755.
[15] D. A. Egger, A. M. Rappe, L. Kronik, *Acc. Chem. Res.* **2016**, *49*, 573.
[16] J. M. Frost, K. T. Butler, F. Brivio, C. H. Hendon, M. van Schilfga arde, A. Walsh, *Nano Lett.* **2014**, *14*, 2584.
[17] L. Z. Tan, F. Zheng, S. M. Young, F. Wang, S. Liu, A. M. Rappe, *npj Comput. Mater.* **2016**, *2*, 16026.
[18] C.-S. Jiang, M. Yang, Y. Zhou, B. To, S. U. Nanayakkara, J. M. Luther, W. Zhou, J. J. Berry, J. van de Lagemaat, N. P. Padture, K. Zhu, M. M. Al-Jassim, *Nat. Commun.* **2015**, *6*, 8397.
[19] X. Wu, L. Z. Tan, X. Shen, T. Hu, K. Miyata, M. T. Trinh, R. Li, R. Coffee, S. Liu, D. A. Egger, I. Makasyuk, Q. Zheng, A. Fry, J. S. Robinson, M. D. Smith, B. Guzelturk, H. I. Karunadasa, X. Wang, X. Zhu, L. Kronik, A. M. Rappe, A. M. Lindenberg, *Sci. Adv.* **2017**, *3*, e1602388.
[20] C. G. Bischak, C. L. Hetherington, H. Wu, S. Aloni, D. F. Ogletree, D. T. Limmer, N. S. Ginsberg, *Nano Lett.* **2017**, *17*, 1028.
[21] A. J. Neukirch, W. Nie, J.-C. Blancon, K. Appavoo, H. Tsai, M. Y. Sfeir, C. Katan, L. Pedesseau, J. Even, J. J. Crochet, G. Gupta, A. D. Mohite, S. Tretiak, *Nano Lett.* **2016**, *16*, 3809.
[22] K. Miyata, D. Meggiolaro, M. T. Trinh, P. P. Joshi, E. Mosconi, S. C. Jones, F. De Angelis, X.-Y. Zhu, *Sci. Adv.* **2017**, *3*.
[23] H. Zhu, K. Miyata, Y. Fu, J. Wang, P. P. Joshi, D. Niesner, K. W. Williams, S. Jin, X.-Y. Zhu, *Science* **2016**, *353*, 1409.
[24] Z. Guo, Y. Wan, M. Yang, J. Snaider, K. Zhu, L. Huang, *Science* **2017**, *356*, 59.
[25] Y. Yang, D. P. Ostrowski, R. M. France, K. Zhu, J. van de Lagemaat, J. M. Luther, M. C. Beard, *Nat. Photonics* **2015**, *10*, 53.
[26] M. B. Price, J. Butkus, T. C. Jellicoe, A. Sadhanala, A. Briane, J. E. Halpert, K. Broch, J. M. Hodgkiss, R. H. Friend, F. Deschler, *Nat. Commun.* **2015**, *6*, 8420.
[27] D. Niesner, H. Zhu, K. Miyata, P. P. Joshi, T. J. S. Evans, B. J. Kudisch, M. T. Trinh, M. Marks, X.-Y. Zhu, *J. Am. Chem. Soc.* **2016**, *138*, 15717.
[28] P. Gu, M. Tani, S. Kono, K. Sakai, X.-C. Zhang, *J. Appl. Phys.* **2002**, *91*, 5533.
[29] S. Casalbuoni, H. Schlarb, B. Schmidt, P. Schmüser, B. Steffen, A. Winter, *Phys. Rev. Spec. Top. – Accel. Beams* **2008**, *11*, 72802.
[30] L. T. Schelhas, J. A. Christians, J. J. Berry, M. F. Toney, C. J. Tassone, J. M. Luther, K. H. Stone, *ACS Energy Lett.* **2016**, *1*, 1007.
[31] V. L. Malevich, R. Adomavičius, A. Krotkus, *C. R. Phys.* **2008**, *9*, 130.
[32] X. C. Zhang, B. B. Hu, J. T. Darrow, D. H. Auston, *Appl. Phys. Lett.* **1990**, *56*, 1011.
[33] M. B. Johnston, D. M. Whittaker, A. Corchia, A. G. Davies, E. H. Linfield, *Phys. Rev. B* **2002**, *65*, 165301.
[34] R. Kersting, K. Unterrainer, G. Strasser, H. F. Kauffmann, E. Gornik, *Phys. Rev. Lett.* **1997**, *79*, 3038.
[35] G. Klatt, F. Hilser, W. Qiao, M. Beck, R. Gebs, A. Bartels, K. Huska, U. Lemmer, G. Bastian, M. B. Johnston, M. Fischer, J. Faist, T. Dekorsy, *Opt. Express* **2010**, *18*, 4939.
[36] K. Reimann, *Rep. Prog. Phys.* **2007**, *70*, 1597.
[37] M. C. Hoffmann, J. A. Fülöp, *J. Phys. D. Appl. Phys.* **2011**, *44*, 83001.
[38] D. W. deQuilettes, S. Koch, S. Burke, R. K. Paranji, A. J. Shropshire, M. E. Ziffer, D. S. Ginger, *ACS Energy Lett.* **2016**, *1*, 438.
[39] J. Lloyd-Hughes, S. K. E. Merchant, L. Fu, H. H. Tan, C. Jagadish, E. Castro-Camus, M. B. Johnston, *Appl. Phys. Lett.* **2006**, *89*, 232102.
[40] S. Olthof, K. Meerholz, *Sci. Rep.* **2017**, *7*, 40267.
[41] P. Gu, M. Tani, *Terahertz Optoelectronics*, Springer, Berlin, Heidelberg **2005**.
[42] G. Giorgi, J.-I. Fujisawa, H. Segawa, K. Yamashita, *J. Phys. Chem. Lett.* **2013**, *4*, 4213.
[43] Q. Dong, Y. Fang, Y. Shao, P. Mulligan, J. Qiu, L. Cao, J. Huang, *Science* **2015**, *347*, 967.
[44] V. Adinolfi, M. Yuan, R. Comin, E. S. Thibau, D. Shi, M. I. Saidaminov, P. Kanjanaboos, D. Kopilovic, S. Hoogland, Z.-H. Lu, O. M. Bakr, E. H. Sargent, *Adv. Mater.* **2016**, *28*, 3406.
[45] J. Shan, T. F. Heinz, in *Ultrafast Dynamical Processes In Semiconductors* Springer Berlin **2004**, pp. 1–56.
[46] M. Sendner, P. K. Nayak, D. A. Egger, S. Beck, C. Mueller, B. Epding, W. Kowalsky, L. Kronik, H. J. Snaith, A. Pucci, R. Lovrincic, *Mater. Horiz.* **2016**, *3*, 613.
[47] T. J. Savenije, A. J. Ferguson, N. Kopidakis, G. Rumbles, *J. Phys. Chem. C* **2013**, *117*, 24085.
[48] O. G. Reid, M. Yang, N. Kopidakis, K. Zhu, G. Rumbles, *ACS Energy Lett.* **2016**, *1*, 561.
[49] A. H. Hill, K. E. Smyser, C. L. Kennedy, E. S. Massaro, E. M. Grumstrup, *J. Phys. Chem. Lett.* **2017**, *8*, 948.
[50] D. M. Monahan, L. Guo, J. Lin, L. Dou, P. Yang, G. R. Fleming, *J. Phys. Chem. Lett.* **2017**, *8*, 3211.
[51] M. A. Pérez-Osorio, R. L. Milot, M. R. Filip, J. B. Patel, L. M. Herz, M. B. Johnston, F. Giustino, *J. Phys. Chem. C* **2015**, *119*, 25703.
[52] A. M. A. Leguy, A. R. Goni, J. M. Frost, J. Skelton, F. Brivio, X. Rodriguez-Martinez, O. J. Weber, A. Pallipurath, M. I. Alonso, M. Campoy-Quiles, M. T. Weller, J. Nelson, A. Walsh, P. R. F. Barnes, *Phys. Chem. Chem. Phys.* **2016**, *18*, 27051.
[53] T. Dekorsy, H. Auer, C. Waschke, H. J. Bakker, H. G. Roskos, H. Kurz, V. Wagner, P. Grosse, *Phys. Rev. Lett.* **1995**, *74*, 738.
[54] M. Tani, R. Fukasawa, H. Abe, S. Matsuura, K. Sakai, S. Nakashima, *J. Appl. Phys.* **1998**, *83*, 2473.
[55] P. Gu, M. Tani, K. Sakai, T.-R. Yang, *Appl. Phys. Lett.* **2000**, *77*, 1798.
[56] A. Leitenstorfer, S. Hunsche, J. Shah, M. C. Nuss, W. H. Knox, *Phys. Rev. Lett.* **1999**, *82*, 5140.
[57] L. M. Herz, *ACS Energy Lett.* **2017**, *2*, 1539.

